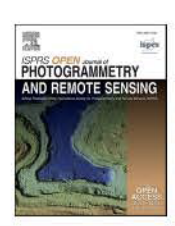
FISEVIER

Contents lists available at ScienceDirect

ISPRS Open Journal of Photogrammetry and Remote Sensing

journal homepage: www.editorialmanager.com/OPHOTO



Monitoring aseismic fault creep using persistent urban geodetic markers generated from mobile laser scanning



Xinxiang Zhu, Ph.D. candidate (Sean) ^{a,*}, Craig L. Glennie, Ph.D., P.Eng. ^a, Benjamin A. Brooks, Ph.D. ^b, Todd L. Ericksen, M.S., P.Eng. ^b

ARTICLEINFO

Keywords:
Mobile laser scanning
Fault creep
Ground displacement detection
RANSAC
Least squares adjustment
Geodetic markers

ABSTRACT

High resolution and high accuracy distributed detection of fault creep deformation remains challenging given limited observations and associated change detection strategies. A mobile laser scanning-based change detection method that is capable of measuring centimeter-level near-field (< 150 m from fault) deformation is described. The methodology leverages the use of man-made features in the built environment as geodetic markers that can be temporally tracked. The proposed framework consists of a RANSAC-based corresponding plane detector and a combined least squares displacement estimator. Using repeat mobile laser scanning data collected in 2015 and 2017 on a 2 km segment of the Hayward fault, near-field fault creep displacement and non-linear creep deformation are estimated. The detection results reveal 2.5 \pm 1.5 cm of accumulated fault parallel creep displacement in the far-field. The laser scanning estimates of displacement match collocated alinement array observations at the 4 mm level in the near field. The proposed change detection framework is shown to be accurate and practical for fault creep displacement detection in the near field and the detected non-linear creep displacement patterns will help elucidate the complex physics of surface faulting.

1. Introduction

Monitoring of aseismic fault creep is important for seismic hazard assessment. Measurements of fault creep displacements can be used to infer locked sections of a fault system which is thought to correspond to the moment magnitude of a seismic event (Lienkaemper et al., 2014; Field et al., 2014). Given the slow-moving characteristics of creep events, surface fault creep monitoring requires the detection of small deformations of the ground surface. Measurements such as creepmeters and static GPS observations over time are commonly used as they can resolve centimeter-level creep rates over temporally spaced observations (McFarland et al., 2016). However, the spatial coverage of these measurements is limited due to the sparse observation network, and the resulting inadequate number of geodetic observations preclude the use of geomechanical models to accurately infer subsurface fault slip and deformation near the Earth's surface (e.g. at infrastructure depths) (Brooks et al., 2017; Nevitt et al., 2020). Mechanically-based modeling of fault creep requires dense near-field observations of surface displacements with broad spatial coverage and high accuracy.

New high-definition photogrammetric and remote sensing surveying techniques like light detection and ranging (lidar), interferometric synthetic aperture radar (InSAR) and uninhabited aerial vehicle synthetic aperture radar (UAVSAR) have recently made it possible to estimate densely distributed ground displacements for the detection of fault dynamics. However, with increased resolution comes complex and irregular formats and measurements with varying accuracy that bring new challenges for change detection, especially in the near field. As a common method of measuring far-field fault displacement, InSAR provides displacement observations with millimeter to centimeter-level accuracy in the far field of the fault (> 1 km distance) (Cakir et al., 2003; Michel et al., 1999; He et al., 2019; Jo et al., 2017; Pepe and Calò, 2017; DeLong et al., 2016). Phase interferometry is highly efficient for observing temporally spaced estimates of deformation in the phase domain, and thus changes can be detected at the millimeter level. However, interferograms tend to decorrelate with spatial change larger than the carrier wavelength and are therefore vulnerable to large displacements and complex textures (e.g. vegetation) found within the near field. This makes InSAR change detection reliable only in the far field (He et al.,

E-mail addresses: xzhu123@uh.edu, zhu123@uh.edu (X. Zhu), clglennie@uh.edu (C.L. Glennie), bbrooks@usgs.gov (B.A. Brooks), tericksen@usgs.gov (T.L. Ericksen).

https://doi.org/10.1016/j.ophoto.2021.100009

a Department of Civil and Environmental Engineering, National Center for Airborne Laser Mapping, University of Houston, Houston, TX, 77204, USA

^b Earthquake Science Center, U.S. Geological Survey, P.O. Box 158, Moffett Field, CA, 94035, USA

^{*} Corresponding author.

2019; Nissen et al., 2014; Michel et al., 1999).

Compared with InSAR, lidar has observational flexibility in the near field even in urban or vegetated areas (Nissen et al., 2014; Scott et al., 2019). Many applications use the iterative closest point method (ICP) and its variants as change detection strategies to reveal fault-related ground displacements (Barnhart et al., 2019; Zhang et al., 2015; Scott et al., 2018, 2020). However, ICP is incapable of resolving gradual centimeter-level changes (Ekhtari and Glennie, 2017) and suffers from higher estimate uncertainties near the fault trace due to the assumption of localized rigid movement (Zhang et al., 2015). These methods cannot be used for estimating fault creep, unless the time horizon between the temporal datasets is large enough to overcome the decimeter-level noise (e.g. Scott et al. (2020)).

There is a paucity of techniques that can provide distributed high accuracy near-field observations over shorter time scales. At the Hayward fault, for example, the slowly creeping characteristics of the fault (a few millimeters per year (McFarland et al., 2016)) have been recorded by alinement array stations and reported annually for decades, but it has not been captured with high spatial resolution. For InSAR, the complex displacement leads to decorrelation that limits the ability to estimate temporally spaced deformation in the phase domain. For lidar, even with high point density, the irregular format of point clouds makes it hard to identify and associate corresponding points that provide consistent estimates of displacement at the point cloud level. Unlike persistent scatterers within an interferogram (Hooper et al., 2004; Crosetto et al., 2016), point cloud based change detection has the flexibility of sensing near-field deformation but the method does not ensure a stable tracking of corresponding features between epochs, and as a result, the application suffers from a matching uncertainty in addition to the errors in the point observations. Therefore, it would be advantageous to develop new methodology for point clouds which include the identification and tracking of geometric features analogous to InSAR persistent scatterers such that reliable geodetic markers can be identified from point clouds and used for change detection in the near field.

In this paper, we propose a change detection strategy using mobile laser scanning (MLS) point clouds that takes advantage of both the steady and gradual movement patterns of the fault creep and the presence of geodetic markers in an urban environment. The method is able to detect distributed fault creep in the near field within approximately 300 m of the fault trace. Fault creep is detected with meter-level resolution and sub-centimeter level accuracy. The proposed method consists of two major parts: (1) a random sample consensus (RANSAC)-based corresponding plane detector, and (2) a combined least squares displacement estimator. The proposed RANSAC-based corresponding plane detector is designed to seek corresponding planar primitives as stable geodetic markers from repeated and temporally spaced MLS scans such that the point clouds representing the same planar objects are segmented together in each epoch of the MLS scan. The nature of the slowly creeping deformation is leveraged for the detector to assign robust correspondence of planar primitives in each MLS dataset. The method is designed to compensate for the incomplete geometrical representation of point clouds due to scan occlusions (Xia et al., 2020), and multiple model fitting problems (Magri and Fusiello, 2016) within point cloud-based change detection.

A combined least squares-based displacement estimator is implemented using the temporally spaced groups of corresponding planar primitives. The adjustment is inspired by the airborne laser scanning (ALS) bore-sight self-calibration model proposed by Skaloud and Lichti (2006). Our previous study (Zhu et al., in press: 11/04/2021) shows that geometric primitive-based change detection using MLS data has the ability to capture centimeter-scale deformation in the fault near field. This work highlights the potential and advantages of augmenting MLS point clouds as geometric primitives for accurate change detection. Point clouds modeled as primitives provide a localization accuracy that is better than the individual lidar point noise (Zhu et al., in press: 11/04/2021). A similar combined least squares adjustment was also

implemented by Kusari et al. (2019) where they showed the method works on large blocks of lidar data. However, the method they proposed is not flexible and robust enough to recover subtle deformation at a resolution finer than the block scale; this makes it insensitive to near-field nonlinear shear displacement patterns (e.g. Chinnery (1961)). In this paper, the use of planar primitives (as geodetic markers) captured from temporally spaced MLS surveys is presented to estimate high accuracy and resolution near-field deformation. Compared with previous work, rather than estimating primitive geometry and ground change separately, the proposed least squares adjustment combines the estimates of displacements with the estimates of primitive geometry, leveraging the additional geometric constraints for estimation of the displacements. The method is able to accurately capture centimeter-level ground deformation and simultaneously estimate primitive geometry thanks to the high degrees of freedom created using planar primitives. The methods are tested on MLS data collected along a 2 km segment of the Hayward fault in 2015 and 2017. The accuracy of the results are validated by the collocated alinement array measurements and fault creep patterns are revealed as displacement fields in the near field of the fault.

The rest of this paper is organized as follows: first the MLS surveys conducted at the Hayward fault are described; then the two-module change detection method is introduced and how the method takes advantage of the characteristics of slow-moving fault creep is demonstrated. Change detection results are then shown and validated with theodolite surveys on collocated alinement arrays. The strength of the regression solutions is then discussed followed by assessments of the change detection strategy.

2. MLS data collection and the Hayward fault

The Hayward fault is known for its active aseismic surface creep and long-timescale geodetic records. Long-term creep rates have been recorded using theodolite surveys since 2001 by the USGS in collaboration with the Geosciences department at SFSU (SFSU creep project homepage, accessed: 10/15/2021). According to their report (McFarland et al., 2016), steady creep rates have been recorded within the MLS surveyed area (Fig. 1). The creep rate at alinement array station HCAM located at Camellia Drive has averaged ~7 mm per year over the past 10 years. Similar creep rates have been recorded at adjacent stations HPMD, HSGR, HONO and HPIN (380 m, 720 m, 980 m and 1000 m from HCAM respectively). Although HPIN and HONO are located outside the survey area, they provide a reliable bound of the creep rates for the MLS survey area. These alinement array measurements outline a steady and gradual dextral slip pattern for the monitored fault creep. Fig. 2 shows accumulated creep observed since 2010 as dextral displacement at these alinement array stations.

The MLS surveys were conducted in July of 2015 and again in June of 2017 near Fremont, CA, along a 2 km segment of the Hayward fault. The survey area is shown in Fig. 1. Two RIEGL VZ-1000 scanners mounted on a pickup truck were used to collect the MLS data with a point density of approximately 300 points/ m^2 at a distance of 20 m from the scanner. Multiple global navigation satellite system (GNSS) base stations were used for data acquisition and all GNSS, inertial navigation system (INS) and laser scanning data was time-tagged and recorded for post-mission analysis with the same survey platform described in Brooks et al. (2017). GNSS/INS data was post processed using Grafnav software in tightly coupled mode. The survey area was primarily devoid of significant vegetation and therefore there was minimal loss of GNSS lock and a comparison of independent forward and reverse GNSS solutions agreed at the centimeter level. Each roadway in the survey area was driven multiple times to minimize occlusions, enable precise boresighting of the laser scanners and provide an internal consistency check for the MLS point clouds. The boresighting was undertaken using a methodology similar to that presented in Skaloud and Lichti (2006). Planar residuals from the boresighting process were examined to ensure that there were no systematic errors present in the MLS trajectory - in general the

map.png

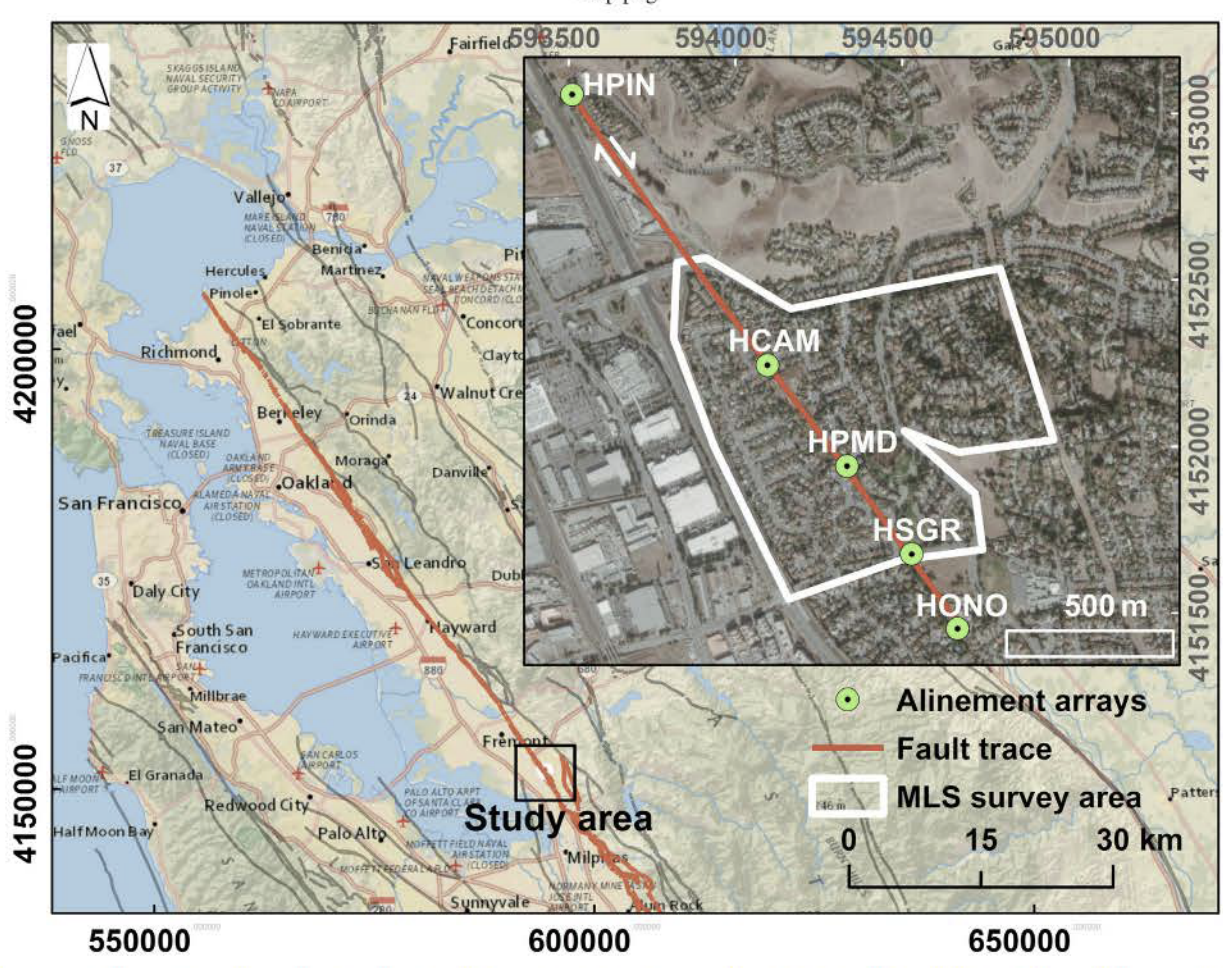


Fig. 1. Maps of the study area. The white polygon outlines the MLS survey extents. The Hayward fault trace is highlighted by the red line and the green dots indicates the alinement stations. (For interpretation of the references to color in this figure legend, the reader is referred to the Web version of this article.)

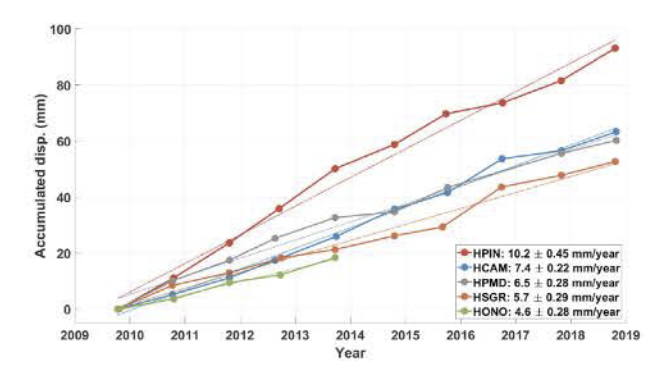


Fig. 2. Accumulated displacement at alinement array stations since 2010. (For interpretation of the references to color in this figure legend, the reader is referred to the Web version of this article.)

root-mean-square error (RMSE) for all planes after boresight adjustment were less than 10 mm. Finally, after boresight adjustment, the areas of overlap in the MLS point cloud were examined to identify any areas with remaining systematic errors by examining vertical profile differences, as the vertical is the weakest component of a GNSS/INS solution. Fig. 3 shows a representative profile (10 cm wide by 90 m) along a flat road approximately 10 m from the scanner. Variations in the point cloud profile show an RMSE of the point cloud (including multiple passes) of less than 10 mm. The careful post-processing and analysis of both the 2015 and 2017 datasets allow us to confidently conclude that the relative

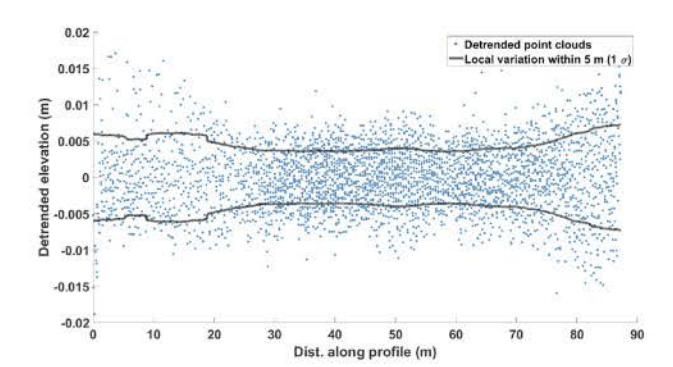


Fig. 3. Vertical profile of the point cloud (10 cm by 90 m) along a roadway. Elevation variation (1 σ) is plotted as a solid line using a 5 m moving window.

noise levels of each of the point clouds are below the expected magnitude of the displacement signal due to fault creep.

3. Methodology

The proposed change detection is executed in two steps. First, a RANSAC-like scheme is developed to find corresponding planar primitives pre- and post-deformation. Second, a combined least squares displacement estimator is used to calculate fault creep displacements constrained by the geometry of the corresponding planar primitives. Details of each process are elaborated below.

3.1. Corr-planar primitives detection

Herein, a planar primitive pre-deformation and its counterpart post-deformation are referred to as the reference and secondary corresponding planar primitives or corr-planar primitives. To find as many corr-planar primitives as possible from repeated MLS observations, we modified the classic RANSAC algorithm (Fischler and Bolles, 1981; Schnabel et al., 2007) that is widely used to extract planar primitives from point clouds. The classic RANSAC detection is improved to run in "parallel" on two or more point clouds collected at the same location with a slightly relaxed consensus threshold for the secondary dataset to compensate for the dislocation induced by motion, in this case, the fault creep. As a result of the creep, a dislocated post-deformation plane is expected to be in a vicinity of the original pre-deformation plane, where the difference between the two is bounded by a relaxed local creep rate estimated from the alinement arrays.

Generally, RANSAC detection of plane features requires four steps: (1) randomly sampling a minimum number of points required to determine the plane, (2) solving for plane parameters given the point samples, (3) calculating the number of inliers for the solved plane with an artificial threshold, and (4) determining if the number of inliers is large enough to justify an update for the plane estimate. To detect corr-planar primitives, the proposed method follows the same steps (1) and (2) performed on the reference point clouds. The improvement lies in the third step where inliers for both the reference and secondary datasets are calculated with a slightly relaxed threshold for the secondary datasets; the plane parameters are only updated when better consensus sets are found in both the reference and secondary sets.

For the modified RANSAC plane detection, both point-to-plane distance and angular deviation to the estimated planes are used as thresholds to calculate the number of inliers. Point-to-plane distances are straightforward to compute, where the normal of each point is estimated by eigendecomposition of its 8-nearest neighbor points as described in the point data abstraction library (PDAL Butler et al. (2021)). For the reference set, point-to-plane distances closer than 3 cm with normal deviations smaller than 7° are counted as inliers; for secondary sets, point-to-plane distances closer than 4 cm with normal deviations smaller than 10° are counted as inliers. These thresholds were calculated by considering the beamwidth of the laser footprint (Glennie, 2007) and the precision of the plane observations. The VZ-1000 scanner has a beam divergence of 0.3 mrad (i.e. laser footprint has a diameter of 3 cm at 100 m), and the precision of the lidar observed planar surfaces are estimated from the ground profile shown in Fig. 3. As shown in Fig. 4, the threshold for a plane |BC| is bounded by the laser point noise estimates of 3 cm for a close range scan (in general < 10 m); distance threshold |CD| is bounded by the creep displacement observed at the alinement array stations,

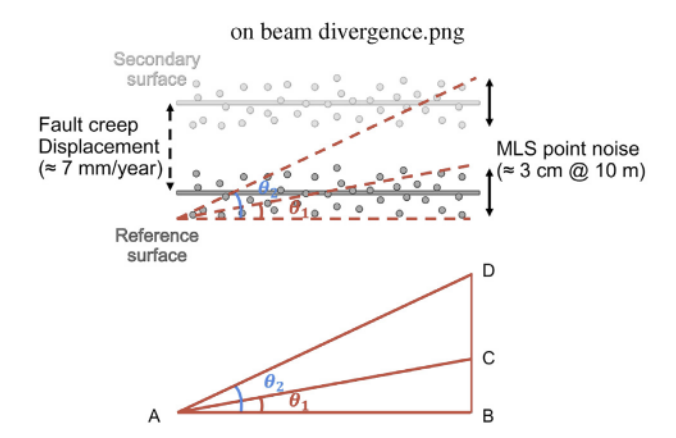


Fig. 4. Illustration of MLS point cloud noise and selection of RANSAC threshold (displacements are not drawn proportionally in this schematic plot).

estimated as 1 cm. The normal vector angular threshold (θ_1, θ_2) is bounded by the smallest plane to be considered such that plane size |AB| larger than $(\frac{|BC|}{\tan \theta_1}, \frac{|BD|}{\tan \theta_2})$ can be detected by the RANSAC detector.

In addition to the RANSAC detector, a sequential searching strategy is also implemented such that the detector is embedded in a moving window looping multiple times through the point clouds. This sequential RANSAC is necessary because multiple planes can be present within a search window, and as a result, a single point may be detected as an inlier on multiple planes. This problem is known as multiple models geometric fitting in computer vision (Magri and Fusiello, 2016).

For each round of RANSAC detection, a subsample of reference dataset query points for the search window is selected where the minimal query point spacing is set to be 0.5 m. The window size is chosen to be 20 m (diameter) which is slightly larger than the biggest planar surface detected within the surveyed neighborhood. As the moving window passes over the dataset, at every query position, the largest corr-planar primitives are detected using the corr-planar RANSAC detector while the affiliation of a point (which plane it belongs to), can be reassigned such that the detection is independent of the query sequence. After looping over all query points, point clouds belonging to the largest planes detected at all query locations are removed and a new round of detection is started to identify and remove point clouds for the second-largest corrplanar primitives. The iterations terminate when there are no corr-planar primitives detected.

A flow chart of the modified RANSAC process can be found in Fig. 5. In this generalized RANSAC detection, the consensus set of a plane consists of all points that are detected as inliers; dually, the preference set of a point consists of all planes that this point potentially belongs to. The reassignment ensures that the point is assigned to the largest consensus set detected within a single round such that large planar objects like walls and roofs will not be broken into patches due to the moving window search; multiple rounds of detection ensure that multiple corr-planes can be captured as long as they are significant enough to contain a minimum amount of points. For this study the minimum point threshold is set to 150 points. The detector captures approximately 60% of the corr-planar primitives within the first iteration using about 40% of the overall processing time and completes detection in an average of 8 iterations.

Fig. 6 demonstrates the detection results of the sequential corr-plane detection where corr-planes are color coded. The method robustly detects corr-planar features. The RANSAC scheme overcomes the incomplete representation of planar geometry in point clouds due to scanning occlusions. In addition, planar primitives are only extracted when counterpart planes exist in the paired dataset.

3.2. Combined least squares adjustment

Given corr-planar primitives extracted from the MLS data, creep deformation can be estimated by re-aligning the corresponding planes using a least squares framework. For fault creep, the deformation is detected as a relative displacement, i.e. how one side of the fault has moved relative to the other side; therefore, precise absolute georeferencing of the two datasets is unnecessary as long as a relative post-registration is performed.

The temporal displacements are estimated based on a least squares adjustment of rigid body transformations conditioned on the planar shape of the corresponding primitives, which is similar to the boresight self-calibration model presented in Skaloud and Lichti (2006). This least squares adjustment estimates the rigid transformation parameters and the plane parameters simultaneously, which is why it is referred to as a combined least squares adjustment. A description of the methods is given below

For any detected corr-planes, given reference point clouds and transformed secondary point clouds, the geometry of the corr-planes are estimated as:

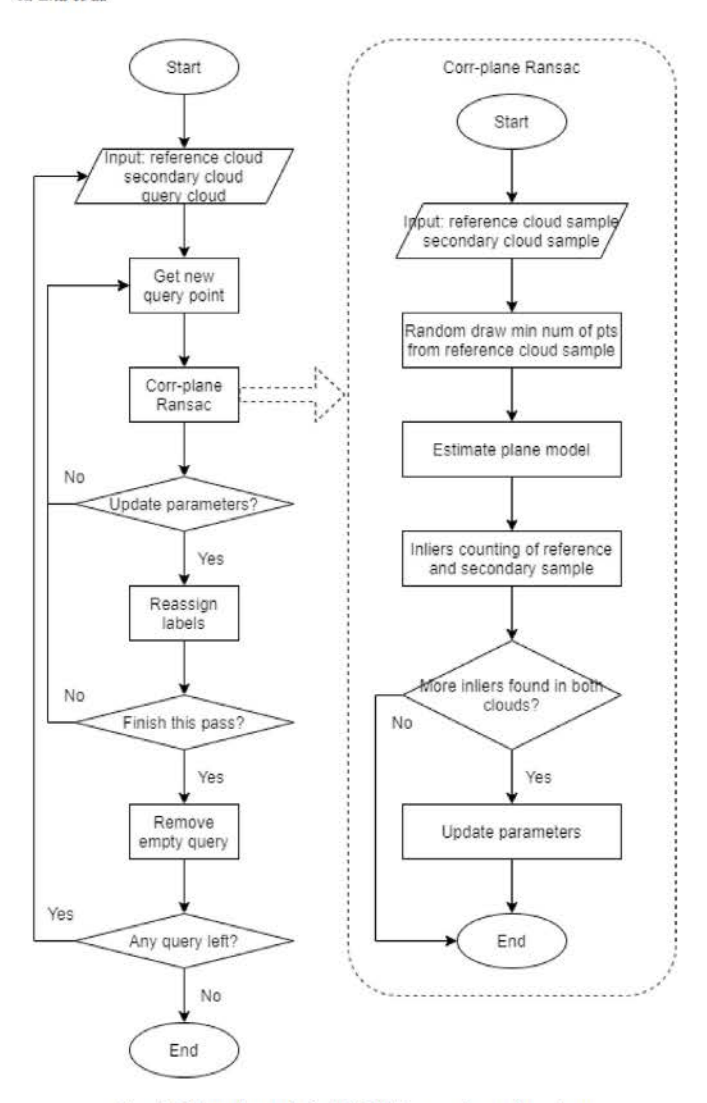


Fig. 5. Flow chart of the RANSAC corr-plane detection.

$$f(l,n,x) = < \begin{bmatrix} n_x \\ n_y \\ n_z \end{bmatrix} \cdot \begin{bmatrix} X \\ Y \\ Z \end{bmatrix} \cdot > = 0$$
 (1)

where $<\cdot>$ represents the dot product of two vectors, and [X, Y, Z] are the coordinates of either the reference or transformed secondary point cloud. Note that both datasets are pre-processed with a constant translation such that the reference point cloud centroid is at the origin.

For secondary point clouds, the rigid transformation assuming small angles (< 1 $\dot{}$) is defined as:

$$\begin{bmatrix} X \\ Y \\ Z \end{bmatrix} = \begin{bmatrix} 1 & -\alpha & \beta \\ \alpha & 1 & -\gamma \\ -\beta & \gamma & 1 \end{bmatrix} \begin{bmatrix} X_s + t_x \\ Y_s + t_y \\ Z_s + t_z \end{bmatrix}$$
(2)

Corr-planes are constrained by geometry:

$$g(n) = n_x^2 + n_y^2 + n_z^2 - 1 = 0 ag{3}$$

In the above equations:

- The observations are l = [l_r; l_s]
 - reference point clouds $l_r = [X_r, Y_r, Z_r]_{obs.}^T$
 - secondary point clouds $l_s = [X_s, Y_s, Z_s]_{abs.}^T$
- The unknowns are n and x
- normal directions of corr-planes $n = (n_x, n_y, n_z)$
- secondary points rigid transformation parameters (3 translations and 3 rotations) $x=(t_x,t_y,t_z,\alpha,\beta,\gamma)$

Given only a single observed plane, the adjustment defined above will be ill-posed because a planar surface is only sensitive to displacement along its normal. To regularize the regression, a group of planes (l_i where i represents plane indices) with varying normal vectors are selected within a query window so that they share a single rigid transformation x in the least squares adjustment. One can visualize this process as the adjustment being implemented on not a single pair of corr-planes but an ensemble consisting of several pairs such that a shared transformation can be estimated and constrained by the geometry of each corr-planar primitive. As long as the augmented planes are not parallel, the geometry of the ensemble is unique enough to ensure a robust regression. By choosing planes randomly within a search radius, the solution's geometry

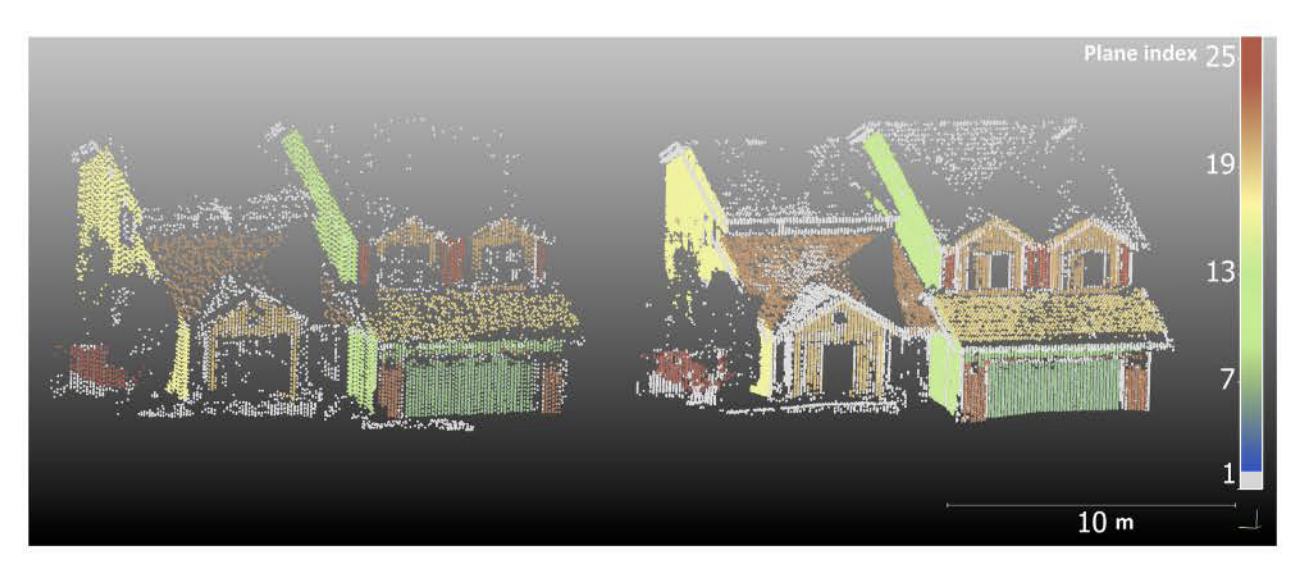


Fig. 6. A sample corr-planar RANSAC detection showing MLS point clouds of a house captured in 2015 (left) and 2017 (right). Points are color coded by index of the corr-planar primitives. Grey points indicate unclassified points which represent either inconsistent objects detected due to MLS scan occlusions or planar primitives that are too small (under 150 pts) to be identified. (For interpretation of the references to color in this figure legend, the reader is referred to the Web version of this article.)

is unique enough to reliably estimate displacement in any direction. The number of planes used for each rigid transformation and the search radius of the query window are empirical parameters that must be chosen based on the density of planar surfaces and their variations in geometry; both of these will be dataset specific. Metrics for selecting the search radius and the number of ensemble planes are discussed in Section 3.3.

A combined adjustment (Gauss-Helmert) model (Mullen, 2004) is used to estimate the solutions. Linearization of Equation (1) and constraint 3 takes the form:

$$A_1\hat{\delta_1} + A_2\hat{\delta_2} + B\hat{v} + w = 0 \tag{4}$$

$$G\hat{\delta}_2 + w_c = v_c \tag{5}$$

where $A_1 = \frac{\partial f}{\partial x}$ and $A_2 = \frac{\partial f}{\partial n}$ are the partial derivative of function f with respect to the unknown transformation and plane parameters, $B = \frac{\partial f}{\partial t}$ is the partial derivative of function f with respect to the observations (laser points), v are the residuals, and w is the misclosure vector, i.e. the value of function f estimated with the estimated parameters and observations. $G = \frac{\partial g}{\partial n}$ is the partial derivative of the constraint g with respect to the unknowns, v_c is the constraint residual vector and w_c is the misclosure vector of the constraints. The adjustment iteratively improves the estimated parameters by the corrections represented by each $\hat{\delta}$, which are the correction vectors for the transformation (1) and plane parameters (2).

Using Lagrange multipliers (λ and μ), Equation (4) can be solved with the constraints provided by Equation (5). The Lagrange function takes the form:

$$\varphi = \hat{v} t P \hat{v} + \hat{v_c} t P_c \hat{v_c} + 2\lambda^t (A_1 \hat{\delta_1} + A_2 \hat{\delta_2} + B \hat{v} + w) + 2\mu^t (G \hat{\delta_2} + w_c - v_c)$$
(6)

here, P and P_c are the corresponding weight matrices, where the diagonal terms are the inverse variance of the observations and constraints, respectively.

Setting the derivatives of the Lagrange function (Equation (6)) equal to zero yields the normal equations given as:

$$\begin{bmatrix} A_{1}^{T}(BP^{-1}B^{T})^{-1}A_{1} & A_{1}^{T}(BP^{-1}B^{T})^{-1}A_{2} \\ A_{2}^{T}(BP^{-1}B^{T})^{-1}A_{1} & A_{2}^{T}(BP^{-1}B^{T})^{-1}A_{2} + G^{T}P_{c}G \end{bmatrix} \begin{bmatrix} \delta_{1} \\ \delta_{2} \end{bmatrix} + \begin{bmatrix} A_{1}^{T}(BP^{-1}B^{T})^{-1}w \\ A_{2}^{T}(BP^{-1}B^{T})^{-1}w + G^{T}P_{c}w_{c} \end{bmatrix} = \begin{bmatrix} 0 \\ 0 \end{bmatrix}$$
(7)

The regression results using Equation (7) lead to simultaneous estimates of displacement (creep) together with corr-planar geometry (planar normals).

3.3. Distribution of corr-planar primitives and strength of least squares solution

Given that displacement is estimated based on the combination of a group of corr-planes within a defined search window, it is meaningful to explore the impact of the ensemble geometry on the regression results. As mentioned previously, a single pair of corr-planes can only be used to detect a displacement in the direction of the plane normal; to capture displacements in all directions a number of closely located corr-planes must be aggregated such that various normal directions are combined. For this aggregation process, the two hyper-parameters to consider, namely the number of corr-planes and the search radius, are actually correlated as they both reflect a general distribution of corr-planes found within the MLS data. An ideal aggregation should take in as many corrplanes as possible to ensure robust solution geometry but within an area as small as possible to have optimal detection resolution. To optimize aggregation geometry while obtaining the highest resolution, an independent measure of the strength of the least squares solution could

be considered. Herein we use an examination of the covariance matrix, similar to the positional dilution of precision (PDOP) metric used in satellite navigation and geomatics engineering (Langley et al., 1999; Santerre et al., 2017) to examine the relative geometric strength of the estimated translation.

To calculate the geometric strength of the translation (GSTR), the trace of the unscaled covariance matrix C_n of the translation parameters is used:

$$C_n = (A^T A)^{-1} \tag{8}$$

$$GSTR = tr(C_n) \tag{9}$$

where A is the Jacobian matrix of Equation (1) with respect to estimated translation $[t_x, t_y, t_z]^T$. GSTR represents the relative strength of the aggregated corr-planes' geometry and is equivalent to PDOP from GNSS processing that evaluates receiver-satellite geometric strength. A larger GSTR corresponds to larger regression uncertainties due to poor geometry (i.e. not a good distribution of planar normals). For example, closely spaced parallel walls and/or roofs could result in large GSTR values indicating weak regression geometry.

Fig. 7 illustrates the distribution of GSTR versus the number of corrplanes for a selection of the Hayward fault MLS data. In this figure, the curve flattens beyond 10 planes as GSTR falls under 10. A conservative minimum of 12 planes is chosen for the proposed combined least squares adjustment. The associated GSTR value (GSTR \approx 2) is used to filter out regression results with weak geometry.

4. Results and interpretations

4.1. Detected fault creep displacement fields

Fig. 8 shows the fault creep displacement field calculated from MLS point clouds acquired in 2015 and 2017. The head of the pin-shaped vector represents where the displacement is detected, and the length and orientation of the pin represent the offset and direction of displacement. Away from the fault, dextral motions are oriented parallel to the fault trace. The average displacement is 1.78 ± 0.8 cm which reflects an average creep magnitude, regardless of orientation, over the entire survey area. However, the amount and direction of the creep displacements vary and show spatial correlation with distance to the fault trace. Note that in the figure we have highlighted those solutions with a GSTR > 2 in red. It is quite clear that the solutions with higher GSTR values contain some outliers as evidenced by their anomalous orientations.

The fault trace presented in Fig. 8 and in subsequent plots is interpolated based on the survey of alinement arrays as documented by McFarland et al. (2016) and SFSU creep project homepage (accessed: 10/15/2021). According to the alinement array surveys, road and curb cracks are used as evidence of the fault location. A connection of these

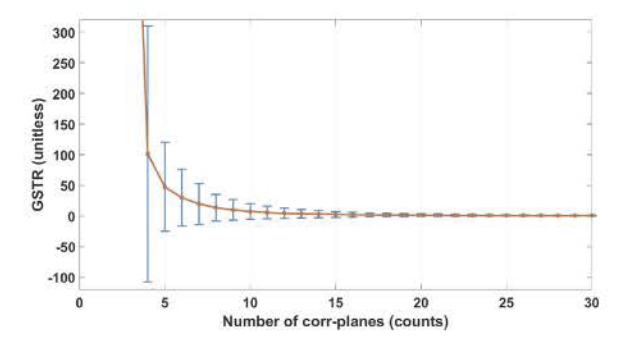


Fig. 7. Geometric strength of the translation (GSTR) versus the number of corrplanes. Error bars show the variation of the distribution calculated over the entire MLS surveyed area.

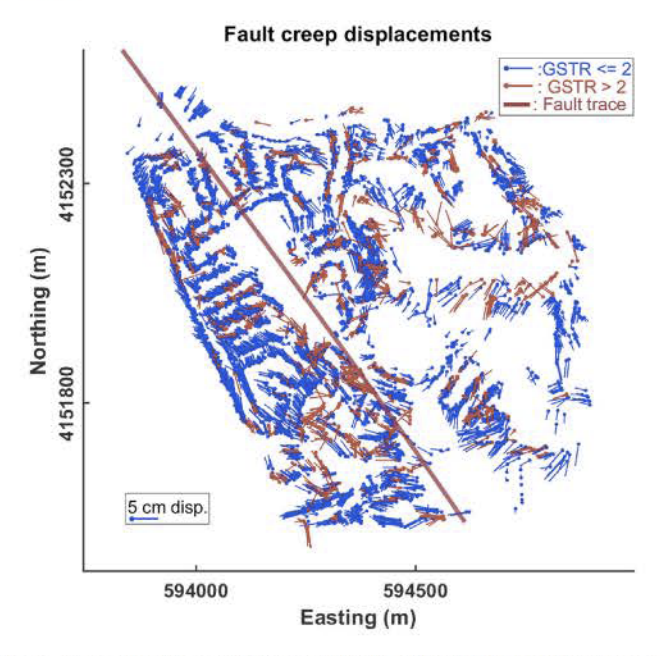


Fig. 8. Detected fault creep displacement field. The field identified fault trace is plotted as the dark red line. Red and blue vectors indicate displacement regression segmented by GSTR (see Section 3.3). (For interpretation of the references to color in this figure legend, the reader is referred to the Web version of this article.)

documented cracks over the region is then used as an estimate of the local fault trace. In this study, local crack measurements at alinement array stations HPIN, HCAM, HPMD, HSGR and HONO are considered as they span the MLS survey area, and the fault trace is estimated as a non-parametric linear local regression (Cleveland, 1979) of the alinement array estimated fault locations. Compared with other records, e.g. Quaternary faults (U.S. Geological Survey and California Geological Survey, accessed: 10/15/2021), this fault trace estimate has better spatial resolution and therefore enhances examination of off-fault creep displacement distributions.

4.2. Distributions of off-fault creep displacements

Using the displacement field and the fault trace estimate, displacements parallel and perpendicular to the fault can be calculated by projecting the displacement vectors along and across the nearest fault trace direction. Fig. 9 shows the spatial distribution of the fault parallel creep displacement; the amount of displacement varies gradually even near the fault trace. This is consistent with the gradual and steady fault creep displacement characteristics reported by field measurements such as McFarland et al. (2016).

Given that the centimeter-level creep displacements along the fault show little variation, it is beneficial to examine displacement profiles across the fault to highlight any off-fault displacement patterns such as fault asymmetry and nonlinear displacements. Fig. 10 shows stacked displacement profiles over the entire MLS surveyed area. These profiles highlight the off-fault variation of fault creep displacements and curvature of the displacement profile that can potentially assist with inferring fault slip at depth (Brooks et al., 2017). In Fig. 10 (a), the fault parallel displacement profile shows curvature within 150 m off-fault and reflects the nonlinear variations of displacement detected in the near field. In the far field, beyond 150 m off-fault, displacements are more uniform, and the overall off-fault dextral displacement is calculated as 2.5 \pm 1.5 cm (1σ) . In Fig. 10 (b) minor fault perpendicular creep is present in the far field with a magnitude of -0.5 ± 1.3 cm (1σ). The scattered displacement records are color coded by GSTR, with inliers colored in blue. The blue dots are clustered around the trend with the remaining colored dots

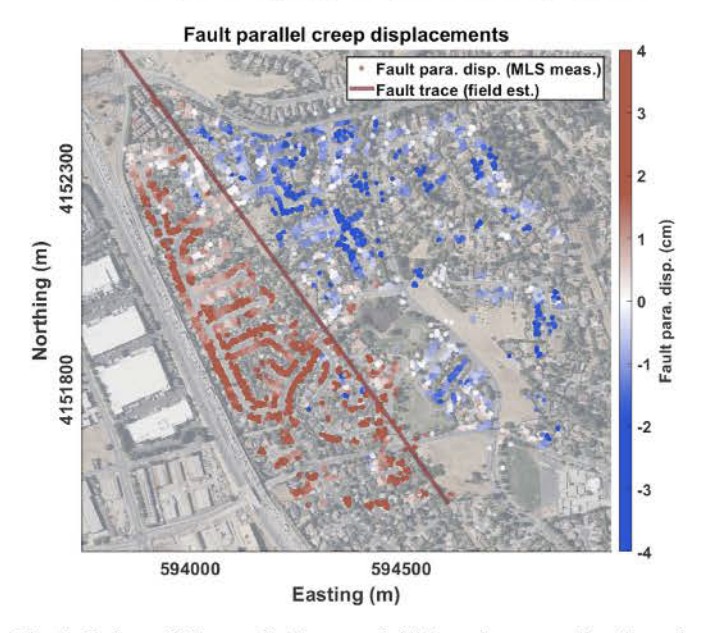


Fig. 9. Fault parallel creep displacement field. Dots show centroids of search window locations for creep colored by the amount of fault parallel displacement. The dark red line indicates the fault trace estimated from the alinement array survey. Basemap from NAIP Digital Georectified Image courtesy of the U.S. Geological Survey (USDA-FSA-APFO et al., 2019). (For interpretation of the references to color in this figure legend, the reader is referred to the Web version of this article.)

spread out with a larger variance within the change detection results. This clustering suggests that GSTR is a good indicator of the strength of the least squares solution and can be used as a filter for robust creep displacement estimates. Only the filtered data (blue dots) contribute to the displacement trend line and error bars shown in both figures; they are computed by binning displacement estimates in 50 m wide bins.

One has to be cautious when interpreting the results in Figs. 9 and 10 because projection accuracy is highly correlated to the definition of the fault trace, which is interpolated based on the field survey of alinement arrays. Although consistent cracks on roads and curbs should be treated as promising evidence of the fault trace, there are limited observations of the ground rupture. Fault slip at depth does not necessarily migrate to the ground surface and deterioration and thermal changes may also lead to scattered cracks that are not necessarily along the strike. Therefore, the fault trace in between surface observations can only be estimated by interpolation and regression. As shown by the distribution in Fig. 9 and the trend in Fig. 10, the 'offset' and the 'plateau' are not perfectly centered on the assumed fault trace (where off-fault distance equals zero). This is also confirmed by some sections of the displacement field in Fig. 8 where the transition zones for the displacement arrows are not centered at the fault trace. Given the discrepancies between these displacement fields and the interpolated fault trace, a more accurate fault trace definition would most likely result in a better estimation of true offfault creep deformation.

The profiles in Fig. 10 enable investigations of fault displacement in the off-fault principle direction; however, the along fault variation of displacements are not evident because the profiles are stacked. Off-fault profiles can be generated at different locations along the fault such that along-fault variations in creep rates can be revealed. Referring to the north end of the MLS survey area as the starting point of the fault trace, along-fault distances are measured and a cascade of off-fault displacement profiles are calculated by sliding a 100 m search window along the fault trace. Fig. 11 shows each profile as a local regression (Cleveland, 1979) of the detected displacements within a window 100 m along and 400 m across the fault. The span of the regression is set at 10% which is equivalent to a 50 m moving average along the displacement profile. In this figure, a minor reduction of fault parallel displacements can be found

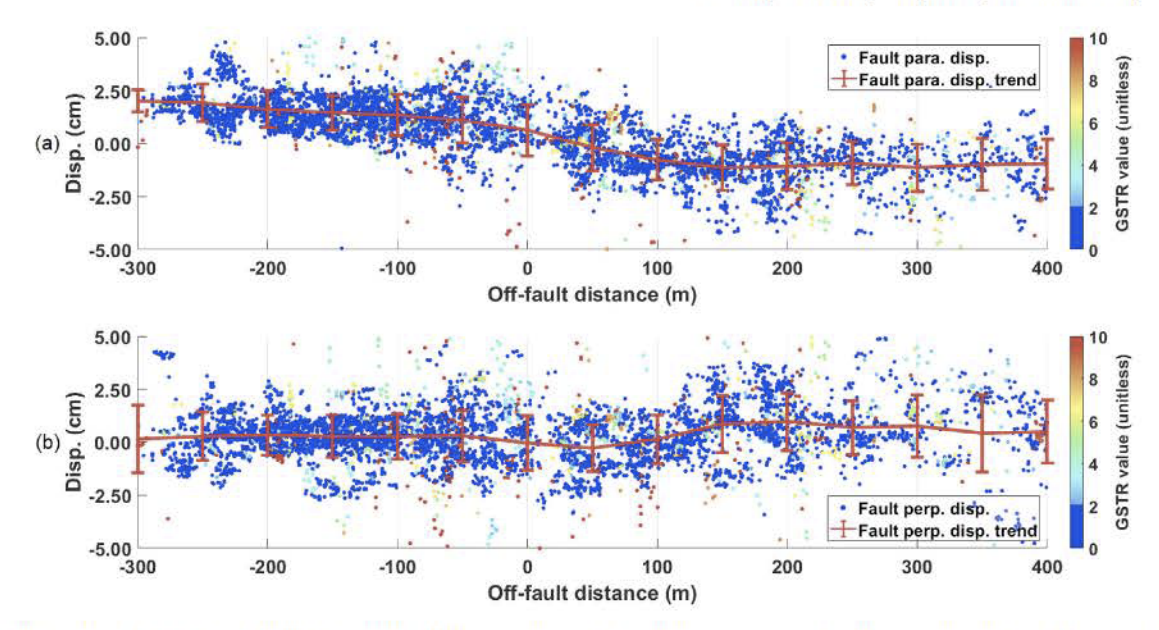


Fig. 10. Distribution of fault parallel (a) and fault perpendicular (b) creep components versus off-fault distance. Trend lines represent a local average of displacements with error bars indicating 50 m binned mean and variance of displacement. Points are color coded by GSTR values to indicate robustness of regression geometry. (For interpretation of the references to color in this figure legend, the reader is referred to the Web version of this article.)

from North to South; this is consistent with the regional trend detected by the alinement arrays (Fig. 3) that spans the area surrounding the MLS survey.

4.3. Validation of the MLS estimates of creep

The Hayward fault is well known for the comprehensive alinement array stations maintained by McFarland et al. (2016). Details of how the alinement array data are collected and processed can be found at the SFSU creep project homepage (accessed: 10/15/2021). The alinement arrays are surveyed with a theodolite such that any fault parallel

movement greater than 1-2 mm can be confidently detected. Here, we use the theodolite surveys of the alinement station HCAM to validate our creep estimates. The location of HCAM can be found in Fig. 1. Although the fault trace is determined by multiple alinement array stations, stations other than HCAM are not compared because they are not covered by persistent MLS observations.

As shown in Fig. 12, the alinement array surveys measure the angular changes of permanent survey monuments located at an alinement station. Dextral fault-parallel creep displacements are then derived from the angular changes. At station HCAM, relative fault parallel displacements are reported at survey monuments IS and ES located 44 m off-fault, and

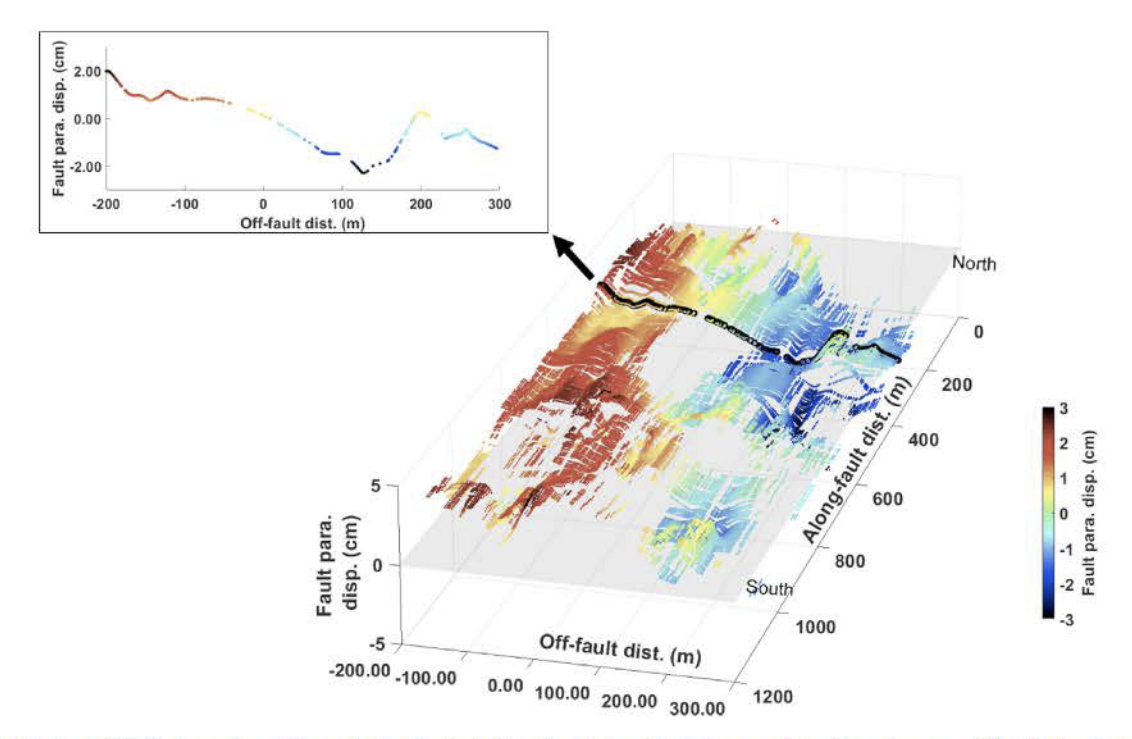


Fig. 11. Off-fault fault parallel displacement profiles stacked along the fault strike. Each profile represents a 50 m binned average of the displacements at various off-fault distances. The cascade of profiles are generated by sliding a 100 m search window along the fault trace with an increment of 5 m. Displacements profiles are colored by the amount of fault parallel creep.

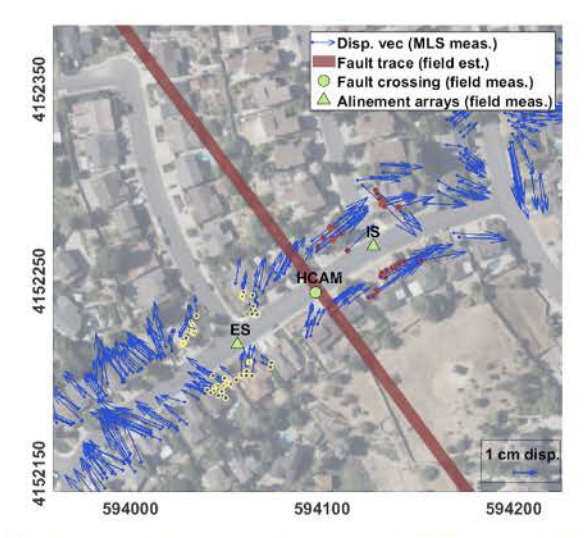


Fig. 12. Displacement field across the fault at alinement station HCAM. The fault trace is shown as the dark red line. The fault crossing at HCAM is marked as a circle and the associated survey monuments IS and ES are marked as triangles. Displacement vectors detected within 20 m of the survey monuments IS and ES are outlined and colored (red-east, yellow-west). Basemap from NAIP Digital Georectified Image courtesy of the U.S. Geological Survey (USDA-FSA-APFO et al., 2019). (For interpretation of the references to color in this figure legend, the reader is referred to the Web version of this article.)

the fault trace is interpolated from adjacent alinement array stations. The equivalent MLS measurement is the relative fault parallel displacements detected around the survey monuments. Fig. 12 displays 20 m wide displacement fields along the line between survey monuments. The corresponding displacement estimates are highlighted with circles and average displacements along the fault are calculated and compared with the theodolite estimates.

The validation results are shown in Fig. 13. In (a), the displacement vectors and the locations of alinement stations are re-plotted with the fault trace centered at the origin and y-axis along the fault trace. The off-fault distributions of fault parallel and fault perpendicular displacements are shown in (b) and (c) and the coincident alignment array measurements are overlaid on (b). Displacement trends are estimated using a robust local linear regression (Cleveland, 1979). Relative dextral displacement is estimated from displacement fields detected 20 m from the survey monuments IS and ES where averaged displacement projections along the fault trace are calculated. At station HCAM, the MLS estimate is $1.1\pm0.7~{\rm cm}~(1\sigma)$ relative dextral displacement from survey monuments IS to ES from July 2015 to June 2017 while the alinement

array survey reports 1.5 \pm 0.7 cm displacement from Oct. 2015 to Oct. 2017. Note that the 4 mm difference between MLS and the alinement array estimates is within the measurement uncertainties of both methods. The difference may be caused by the slightly different observation periods for each. As shown in the long term records for HCAM and adjacent stations (Fig. 2), the creep rate along the Hayward fault is not constant and can vary by several millimeter per year.

It also appears, based on the profiles in Fig. 13 that the HCAM alinement array stations are within the fault zone of deformation and therefore may not completely capture the off-fault creep deformation. A localized rotation of the MLS displacement vectors can be found between $-10\,$ m and $50\,$ m off-fault. The orientation of the vectors is almost perpendicular to the fault trace. The rotation is also captured in the fault perpendicular displacement profile in Fig. 13 (c). A second profile minima is observed between 130 m and 170 m off-fault from a similar rotational pattern. This second local minimum suggests that the alinement array monument IS is located within the deformation zone while the ES-IS baseline does not span the entire creeping zone. To confirm that these detected rotational patterns are not a consequence of the smoothing induced by the moving window employed, a synthetic test was conducted, with details presented in Section 4.4.

4.4. Detection of synthetic creep

To better understand the uncertainties of the proposed change detection strategy, a synthetic test was undertaken with a synthesized fault creep. In the synthetic configuration, reference and secondary datasets were generated by randomly drawing two point clouds from the 2015 MLS data, and adding a 4 cm rigid dextral displacement with dislocation at the fault trace to one of the point clouds. This offset matches the scale of the expected far-field displacement. The displacement configuration also ensures an upper bound of the fault creep as the near-field displacement accommodates all the far-field fault slip instantly at the fault trace.

Figs. 14 and 15, show example profiles near HCAM with the 4 cm synthetic dislocation. The synthetic results show a 0.2 cm variation represented by the thickness of the displacement profile. A smoothing effect induced by the moving window can be found ± 10 m off-fault where the simulated stair-like displacement is detected as a linear transition off-fault. No bias in the direction of the detected displacements are shown in Fig. 16, and the angular variation of the vectors is only 10° (1σ).

The synthetic results show that the selection window for the planes has only a minimal smoothing effect on the estimate of displacement as it crosses the simulated fault location. The window size does not seem to affect the estimated displacement direction significantly. It is, therefore, highly unlikely that the transition width displayed in Fig. 13, which

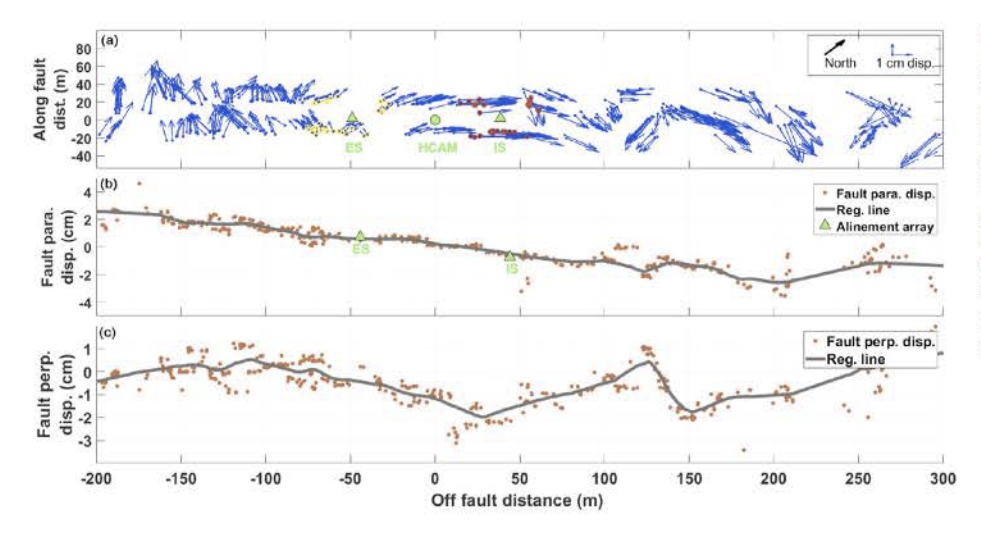


Fig. 13. Displacement profiles estimated by MLS at alinement station HCAM. (a) Detected displacement fields viewed from an off-fault perspective (centered at the fault trace and rotated by the strike direction). Corresponding displacement vectors for survey monuments IS and ES are circled. Labels for HCAM, IS and ES are the same as Fig. 12. (b) Profile of the fault parallel displacement overlaid with coincident alinement array measurements. Y-offset of survey monuments represents the dextral displacements detected by the alinement array over the same approximate time period. (c) Profile of the fault perpendicular displacement.

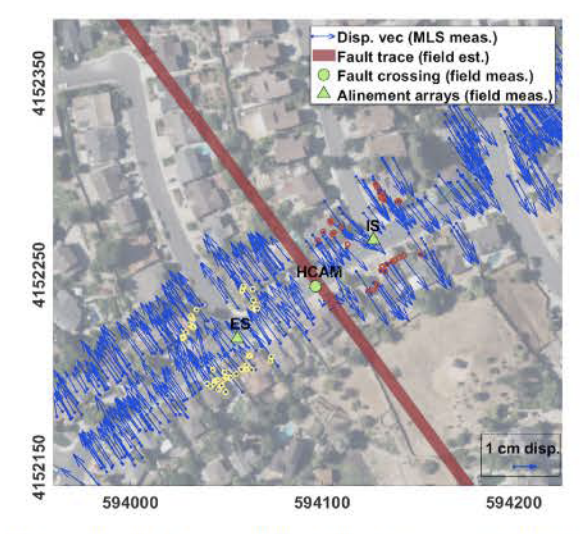


Fig. 14. Synthetic displacement field at alinement station HCAM. Basemap from NAIP Digital Georectified Image courtesy of the U.S. Geological Survey (USDA-FSA-APFO et al., 2019).

appears to be at least 50 m wide with a noticeable systematic rotation pattern, is caused by the size of the selection window.

5. Discussion

5.1. Generality of the proposed change detection strategy

The structure of the proposed two-step strategy leads to a general framework for change detection not limited by the type of fault, the deformation rate or the primitive geometry. The method detects changes in 3D; vertical changes can also be estimated for a non strike-slip fault. In the first step, implementation of the RANSAC corr-planar detector leverages the slow deformation characteristics of the fault creep where the secondary point clouds are expected to be nearly adjacent to the reference point clouds. The method would still be feasible without the assumption of slow deformation as alternatively, a coarse alignment (like ICP) could first be applied either globally or locally. The RANSAC detector could then be implemented with the consensus threshold adjusted accordingly based on the estimated accuracy of the ICP solution. The selection of geodetic marker type can also be adapted to other geometric primitive besides planar surfaces. The 'parallel' consensus threshold and

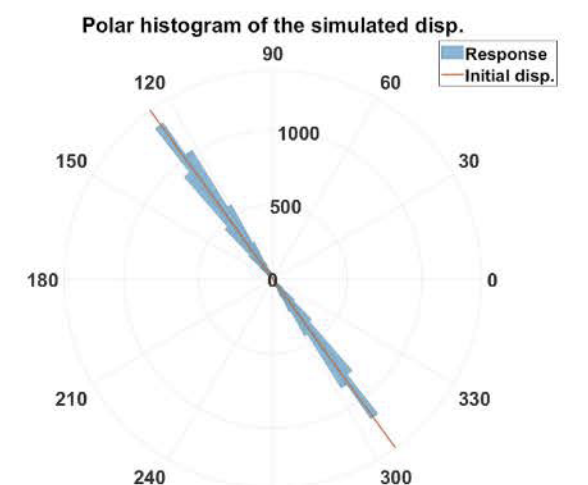


Fig. 16. Angular histogram of the detected displacement vector orientation. Actual displacement directions are plotted as the red line representing the average strike of the fault trace. The angular histogram of the detected displacement directions shows no bias from the actual directions as the bins are centered on the red line. (For interpretation of the references to color in this figure legend, the reader is referred to the Web version of this article.)

270

the sequential RANSAC strategy can be applied to other types of corresponding geometric primitives such as concentric cylinders and spheres.

In the second step, the combined least squares adjustment framework can also be augmented to incorporate different types of primitives. Equation (1) can be generalized to combined primitives of various types conditioned by their own geometry as shown in Equation (3), and the estimate on the rigid transformation remains as shown in Equation (2). By using a wider variety of geometric primitives, the geometry of the geodetic markers will be more distinctive and should improve the regression geometry GSTR and accuracy. The smoothing effect induced by the moving window search would also be suppressed as a smaller search window can be used with a wider selection of candidate primitive types. This type of generalized geometric primitive framework is already planned to augment the approach presented.

The proposed two-module strategy can be extended to estimate change for faulting outside of urban neighborhoods. The detection using corr-planar primitives is practical and feasible as planar surfaces are abundant in urban areas. However, the environment demonstrated in this

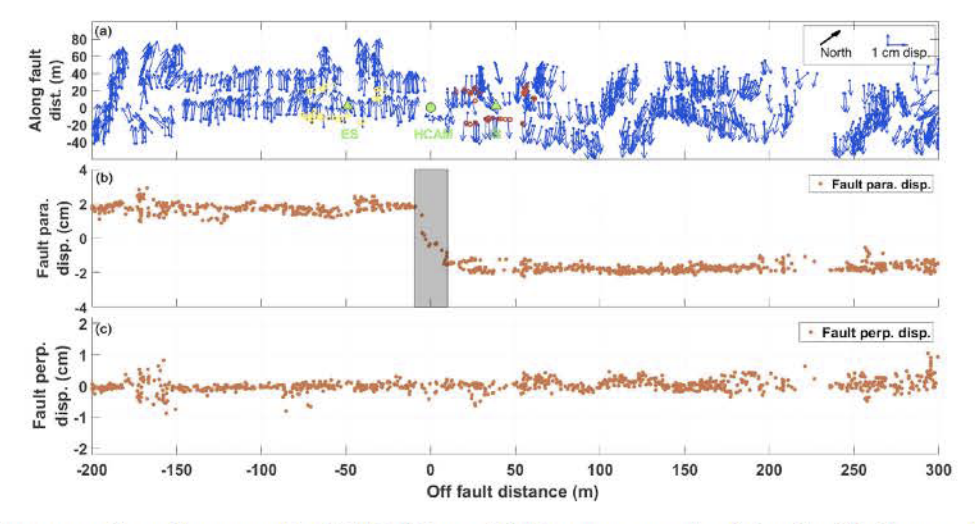


Fig. 15. Synthetic displacement profiles at alinement station HCAM. (a) Detected displacement vectors viewed from the off-fault perspective (centered at the fault trace and rotated by the strike direction). (b) Profile of fault parallel displacement. The grey rectangle highlights the 20 m transition zone due to the smoothing effect of the moving window. (c) Profile of fault perpendicular displacement. Profiles in (b) and (c) show variations of approximately 2 mm overall.

project is relatively simple as repeated houses in the same neighborhood contribute most of the planar features for change detection. As planar surfaces can be extracted from buildings or other types of constructions at various sizes with different scan uncertainties, static thresholds implemented by this project may not be optimized for different anthropogenic environments. Besides scan uncertainties, construction materials on facades and roofs of a building may also introduce additional roughness or curvature that needs to be considered for the RANSAC corr-planar detection. Further parameter tuning and adjustment is necessary to implement this method in different environments. Generalizing the method to be scene invariant will require the examination of more datasets collected in differing environments.

The dense measurements of fault creep clearly highlight the benefit of MLS high-resolution change detection. The mobile platform provides a side-looking scan that enables better point-cloud definition of vertical features which is ideal for measuring horizontal deformation. Other techniques, such as structure from motion digital imaging could also potentially be used to provide the input point clouds for change detection (e.g. Ekhtari and Glennie (2017)). If the images were acquired from airborne platforms (e.g. UAS platform) then they may provide more uniform coverage as their acquisition is not limited to the roadways, although potential occlusions by vegetation may limit their use in some areas. There may also be some issues because the structure from motion/multiview stereo photogrammetry (SfM-SVS) process tends to round sharp edges (Slocum and Parrish, 2017) which may deform the planar surfaces being used for estimating deformation.

6. Conclusion and future work

Herein, an MLS-based change detection framework to monitor the slow deformation of aseismic fault creep along a segment of the Hayward fault has been described. The fault deformation was elucidated as displacement vectors with meter-level resolution and sub-centimeter accuracy. The detected displacement vectors show nonlinear deformation patterns in the near field and $2.5\pm1.5~\rm cm$ dextral displacement in the far field (> 150 m off-fault). Rotational patterns are detected within the nonlinear deformation zone close to the fault. The magnitude of creep displacement estimated was validated using a collocated alinement array station with millimeter-level agreement. The detected displacement fields can be used to elucidate the complex physics of faulting near the Earth's surface and the nonlinear deformation pattern and the scale of off-fault displacement can be used as a reference to set up future geodetic and geophysical networks for monitoring fault dynamics.

The two-step change detection strategy was shown to be practical and feasible. The RANSAC-based corresponding planes detector seeks corresponding temporally spaced geodetic markers by leveraging the slow deformation characteristics of fault creep, and the combined least squares displacement estimator is used to quantify both the relative fault creep displacement and the regression of the primitive geometry simultaneously.

The change detection method was assessed from the perspective of the reliability of the geodetic markers, the smoothing effect of the moving window detection, and the potential generalization of the framework. GSTR was shown to be a practical metric to quantify the robustness of the regression geometry. A conservative test using a synthetic fault displacement shows approximately 2 mm detection uncertainties for dextral slip, 10° angular uncertainties in displacement orientation, and ± 10 m off-fault smoothing caused by the size of the planar selection window.

For future work, we plan to generalize the choice of geodetic markers such that non-planar primitives can also be used to track deformation. We also plan to use multiple temporally spaced MLS surveys in a simultaneous adjustment network to further improve the accuracy and reliability of the creep estimates.

Acknowledgements

Partial funding for this research was provided by a cooperative agreement from the USGS and two grants from the National Science Foundation (1347092 and 1830734). We would also like to thank the three anonymous reviewers whose constructive criticism greatly improved the final manuscript.

References

- Barnhart, W.D., Gold, R.D., Shea, H.N., Peterson, K.E., Briggs, R.W., Harbor, D.J., 2019. Vertical coseismic offsets derived from high-resolution stereogrammetric DSM differencing: the 2013 Baluchistan, Pakistan earthquake. J. Geophys. Res.: Solid Earth 124 (6), 6039–6055.
- Brooks, B.A., Minson, S.E., Glennie, C.L., Nevitt, J.M., Dawson, T., Rubin, R., Ericksen, T.L., Lockner, D., Hudnut, K., Langenheim, V., et al., 2017. Buried shallow fault slip from the South Napa earthquake revealed by near-field geodesy. Sci. Adv. 3 (7), e1700525.
- Butler, H., Chambers, B., Hartzell, P., Glennie, C., 2021. PDAL: an open source library for the processing and analysis of point clouds. Comput. Geosci. 148, 104680.
- Cakir, Z., Chabalier, J.-B. d., Armijo, R., Meyer, B., Barka, A., Peltzer, G., 2003. Coseismic and early post-seismic slip associated with the 1999 Izmit earthquake (Turkey), from SAR interferometry and tectonic field observations. Geophys. J. Int. 155 (1), 93–110.
- Chinnery, M., 1961. The deformation of the ground around surface faults. Bull. Seismol. Soc. Am. 51 (3), 355–372.
- Cleveland, W.S., 1979. Robust locally weighted regression and smoothing scatterplots. J. Am. Stat. Assoc. 74 (368), 829–836.
- Crosetto, M., Monserrat, O., Cuevas-González, M., Devanthéry, N., Crippa, B., 2016.
 Persistent scatterer interferometry: a review. ISPRS J. Photogrammetry Remote Sens.
 115, 78–89.
- DeLong, S.B., Donnellan, A., Ponti, D.J., Rubin, R.S., Lienkaemper, J.J., Prentice, C.S., Dawson, T.E., Seitz, G., Schwartz, D.P., Hudnut, K.W., et al., 2016. Tearing the terroir: details and implications of surface rupture and deformation from the 24 August 2014 M6. 0 South Napa earthquake, California. Earth Space Sci. 3 (10), 416–430.
- Ekhtari, N., Glennie, C.L., 2017. High-resolution mapping of near-field deformation with airborne Earth observation data, a comparison study. IEEE Trans. Geosci. Rem. Sens. 56 (3), 1598–1614.
- Field, E.H., Arrowsmith, R.J., Biasi, G.P., Bird, P., Dawson, T.E., Felzer, K.R., Jackson, D.D., Johnson, K.M., Jordan, T.H., Madden, C., et al., 2014. Uniform California earthquake rupture forecast, version 3 (UCERF3)—the time-independent model. Bull. Seismol. Soc. Am. 104 (3), 1122–1180.
- Fischler, M.A., Bolles, R.C., 1981. Random sample consensus: a paradigm for model fitting with applications to image analysis and automated cartography. Commun. ACM 24 (6), 381–395.
- Glennie, C., 2007. Rigorous 3D error analysis of kinematic scanning lidar systems. J. Appl. Geodes. 1 (3), 147–157.
- He, P., Wen, Y., Xu, C., Chen, Y., 2019. Complete three-dimensional near-field surface displacements from imaging geodesy techniques applied to the 2016 Kumamoto earthquake. Rem. Sens. Environ. 232, 111321.
- Hooper, A., Zebker, H., Segall, P., Kampes, B., 2004. A new method for measuring deformation on volcanoes and other natural terrains using InSAR persistent scatterers. Geophys. Res. Lett.
- Jo, M.-J., Jung, H.-S., Yun, S.-H., 2017. Retrieving precise three-dimensional deformation on the 2014 M6. 0 South Napa earthquake by joint inversion of multi-sensor SAR. Sci. Rep. 7 (1), 1–10.
- Kusari, A., Glennie, C.L., Brooks, B.A., Ericksen, T., 2019. Precise registration of laser mapping data by planar feature extraction for deformation monitoring. IEEE Trans. Geosci. Rem. Sens. 57 (6), 3404–3422.
- Langley, R.B., et al., 1999. Dilution of precision. GPS World 10 (5), 52-59.
- Lienkaemper, J.J., McFarland, F.S., Simpson, R.W., Caskey, S.J., 2014. Using surface creep rate to infer fraction locked for sections of the San Andreas fault system in northern California from alignment array and GPS data. Bull. Seismol. Soc. Am. 104 (6), 3094–3114.
- Magri, L., Fusiello, A., 2016. Multiple model fitting as a set coverage problem. In: Proceedings of the IEEE Conference on Computer Vision and Pattern Recognition (CVPR), pp. 3318–3326.
- McFarland, F.S., Lienkaemper, J.J., Caskey, S.J., 2016. Data from theodolite measurements of creep rates on San Francisco Bay region faults, California (version 1.8, march 2016): U.S. Geological Survey open-file report 2009–1119, p. 21 (p. and data files).
- Michel, R., Avouac, J.-P., Taboury, J., 1999. Measuring near field coseismic displacements from SAR images: application to the Landers earthquake. Geophys. Res. Lett. 26 (19), 3017–3020.
- Mullen, R., 2004. Manual of Photogrammetry. Asprs Publications.
- Nevitt, J.M., Brooks, B.A., Catchings, R.D., Goldman, M.R., Ericksen, T.L., Glennie, C.L., 2020. Mechanics of near-field deformation during co-and post-seismic shallow fault slip. Sci. Rep. 10 (1), 1–13.
- Nissen, E., Maruyama, T., Arrowsmith, J.R., Elliott, J.R., Krishnan, A.K., Oskin, M.E., Saripalli, S., 2014. Coseismic fault zone deformation revealed with differential lidar: examples from Japanese Mw ~ 7 intraplate earthquakes. Earth Planet Sci. Lett. 405, 244–256.

- Pepe, A., Calò, F., 2017. A review of interferometric synthetic aperture RADAR (InSAR) multi-track approaches for the retrieval of Earth's surface displacements. Appl. Sci. 7 (12), 1264.
- Santerre, R., Geiger, A., Banville, S., 2017. Geometry of GPS dilution of precision: revisited. GPS Solut. 21 (4), 1747–1763.
- Schnabel, R., Wahl, R., Klein, R., 2007. Efficient RANSAC for point-cloud shape detection. In: Computer Graphics Forum, vol. 26. Wiley Online Library, pp. 214–226.
- Scott, C., Champenois, J., Klinger, Y., Nissen, E., Maruyama, T., Chiba, T., Arrowsmith, R., 2019. The 2016 M7 Kumamoto, Japan, earthquake slip field derived from a joint inversion of differential lidar topography, optical correlation, and InSAR surface displacements. Geophys. Res. Lett. 46 (12), 6341–6351.
- Scott, C.P., Arrowsmith, J.R., Nissen, E., Lajoie, L., Maruyama, T., Chiba, T., 2018. The M7 2016 Kumamoto, Japan, earthquake: 3-D deformation along the fault and within the damage zone constrained from differential lidar topography. J. Geophys. Res.: Solid Earth 123 (7), 6138–6155.
- Scott, C.P., DeLong, S.B., Arrowsmith, J.R., 2020. Distribution of assismic deformation along the Central San Andreas and Calaveras faults from differencing repeat airborne lidar. Geophys. Res. Lett. 47 (22) e2020GL090628.

- SFSU creep project homepage, 10/15/2021. http://funnel.sfsu.edu/creep/.
- Skaloud, J., Lichti, D., 2006. Rigorous approach to bore-sight self-calibration in airborne laser scanning. ISPRS J. Photogrammetry Remote Sens. 61 (1), 47–59.
- Slocum, R.K., Parrish, C.E., 2017. Simulated imagery rendering workflow for UAS-based photogrammetric 3D reconstruction accuracy assessments. Rem. Sens. 9 (4), 396.
- U.S. Geological Survey and California Geological Survey, 10/15/2021. Quaternary fault and fold database for the United States. https://www.usgs.gov/natural-hazar ds/earthquake-hazards/faults.
- USDA-FSA-APFO, et al., 2019. NAIP Digital Georectified Image.
- Xia, S., Chen, D., Wang, R., Li, J., Zhang, X., 2020. Geometric primitives in lidar point clouds: a review. IEEE J. Select. Topic. Appl. Earth 13, 685–707.
- Zhang, X., Glennie, C., Kusari, A., 2015. Change detection from differential airborne lidar using a weighted anisotropic iterative closest point algorithm. IEEE J. Select. Topic. Appl. Earth 8 (7), 3338–3346.
- Zhu, X., Glennie, C.L., Brooks, B.A., 2021. Automated near-field deformation detection from mobile laser scanning for the 2014 Mw 6. 0 South Napa earthquake. J. Appl. Geodes.